Aero-elastic simulations using the NSMB CFD solver including results for a strut braced wing aircraft

Vos, J. B.; Charbonnier, D.; Ludwig, T.; Merazzi, S.; Timmermans, H.; Rajpal, D.; Gehri, A.

DOI
10.1007/978-3-030-36514-1_5

Publication date
2020

Document Version
Final published version

Published in
Lecture Notes in Applied and Computational Mechanics

Aero-elastic Simulations Using the NSMB CFD Solver Including results for a Strut Braced Wing Aircraft

J. B. Vos, D. Charbonnier, T. Ludwig, S. Merazzi, H. Timmermans, D. Rajpal and A. Gehri

Abstract More then 10 years ago a large investment was made in extending the NSMB Navier Stokes Multi Block (NSMB) Computational Fluid Dynamics (CFD) towards Fluid Structure Interaction (FSI) simulations (Guillaume et al. in Fluid structure interaction simulation on the F/A-18 vertical tail, 2010 [1], Guillaume et al. in Aeronaut J 115:285–294, 2011 [2]). At that time a segregated approach was adopted using a loosely coupled approach. More recently NSMB was coupled to the open-source Finite Element Analysis environment B2000++ (http://www.smr.ch/products/b2000/ [3]) in a strongly coupled approach. This has led to the possibility to perform both static and dynamic FSI simulations using either a modal or a FEM approach without the need to interrupt the simulation. Results of aero-elastic simulations for the MDO-aircraft, the AGARD445.6 wing and for a Strut Braced Wing configuration will be presented.

J. B. Vos (✉) · D. Charbonnier
CFS Engineering, EPFL Innovation Park, Batiment A, 1015 Lausanne, Switzerland
e-mail: jan.vos@cfse.ch

D. Charbonnier
e-mail: dominique.charbonnier@cfse.ch

T. Ludwig · S. Merazzi
SMR Engineering and Development, Blumenstrasse 14-16, 2502 Bienne, Switzerland
e-mail: tludwig@smr.ch

S. Merazzi
e-mail: merazzi@smr.ch

H. Timmermans
NLR Netherlands Aerospace Centre, Postbus 90502, 1006 BM Amsterdam, The Netherlands
e-mail: Huub.Timmermans@nlr.nl

D. Rajpal
Delft University of Technology Faculty of Aerospace Engineering,
Kluyverweg 1, 2629 Delft, The Netherlands
e-mail: D.Rajpal@tudelft.nl

A. Gehri
Aerodynamics Department, RUAG Aviation, 6032 Emmen, Switzerland
e-mail: alain.gehri@ruag.com

M. E. Biancolini and U. Cella (eds.), *Flexible Engineering Toward Green Aircraft*,
Lecture Notes in Applied and Computational Mechanics 92,
https://doi.org/10.1007/978-3-030-36514-1_5

1 Introduction

The Swiss Airforce operates since 1997 the F/A-18 C/D fighter. The usage of this aircraft is about three times more severe than the original design, requiring changes in the aircraft structure. To better understand the aerodynamic loads on the aircraft RUAG Aviation made a large investment in extending the Navier Stokes Multi Block (NSMB) Computational Fluid Dynamics (CFD) code to allow for Fluid Structure Interaction (FSI) simulations [1, 2]. Procedures were developed for both static and dynamic Fluid Structure Interaction. Static Fluid Structure Interaction was put in place using a segregated two solver approach. A CFD calculation was made and run for a certain number of steps, the calculation was stopped, the aerodynamic loads were extracted and used as input for Nastran. Nastran computed the displacements of the aircraft structure that were transformed to surface grid point displacements. The CFD solver was then re-started and used these displacements to re-compute the grid, and then continued the calculation on this new grid, typically for about 300–500 steps. Then the CFD solver was stopped and the process was repeated. In general 4 to 5 of these iterations were made to obtain a converged deformed geometry.

Dynamic FSI simulations were made for the F/A-18 C/D fighter to study vertical tail buffeting, and employed a linear structural model based on a modal formulation. In this case the CFD solver and the Computational Structural Mechanics (CSM) solver are tightly coupled [1].

Over the past years several developments were made that are presented in this paper. The NSMB CFD solver was extended with the chimera method that permits easy changes of control surface deflections and that facilitates the mesh generation for complex geometries. The need to provide quickly aerodynamic loads for statically deformed wings led to the decision to couple the NSMB CFD solver with the open-source Finite Element Analysis environment B2000++ [3]. This has led to the possibility to perform both static and dynamic FSI simulations using either a modal or a FEM approach without the need to interrupt the simulation.

This paper is organized as follows: first the CFD solver NSMB and the FEM Environment B2000++ are briefly presented. This is followed by a more detailed discussion on the different elements of the aero-elastic simulation environment. This environment has been validated using two known test cases, the MDO Aircraft [4] and the GARD445.6 wing [5]. Finally, in the frame of the EU funded H2020 project AGILE [6], the aero-elastic simulation environment was used to compute a Strut Braced Wing aircraft. Other approaches and methods for fluid structure interaction simulations can be found in the literature [7–9].

2 The NSMB CFD Solver

The Navier Stokes Multi Block solver NSMB was initially developed in 1992 at the Swiss Federal Institute of Technology (EPFL) in Lausanne, and from 1993 onwards in the NSMB consortium composed of different universities, research establishments

and industries. Today NSMB is developed by IMF-Toulouse (IMFT, France), ICUBE (Strasbourg, France), University of Munchen (TUM, Germany), University of the Army in Munchen (Germany), Ariane Group (France), RUAG Aviation and CFS Engineering. A variety of papers have been published on NSMB, examples are in [1, 10–13].

NSMB is a parallelized CFD solver employing the cell-centered finite volume method using multi block structured grids to discretize the Navier Stokes equations. To simplify the mesh generation for complex geometries NSMB uses the patch grid (also known as the sliding mesh) approach and the chimera method. The chimera method is also used for simulations involving moving bodies.

Space discretization schemes implemented in NSMB are the 2nd and 4th order central schemes with artificial dissipation and Roe and AUSM upwind schemes from 1st to 5th order. Time integration can be made using explicit Runge-Kutta schemes, or the semi-implicit LU-SGS scheme. Different methods are available to accelerate the convergence to steady state, as for example local time stepping, multigrid and full multigrid, and low Mach number preconditioning. Unsteady simulations are made using the dual time stepping approach or using the 3rd order Runge Kutta scheme.

Turbulence is modelled using standard approaches as for example the algebraic Baldwin-Lomax model, the 1-equation Spalart model [14] (and several of it's variants) and the $k - \omega$ family of models (including the Menter Shear Stress model [15]). Explicit Algebraic Reynolds Stress models and Reynolds Stress models have also been implemented, but are not used on a routine base. Transition to turbulence can be modelled by specifying transition lines or planes, or by solving the $\gamma - R_\theta$ transport equations [16]. For unsteady CFD simulations different Hybrid RANS-LES models are available.

The Arbitrary Langerian Eulerian (ALE) approach is employed for simulations using moving or deforming grids. When using the ALE approach it is not necessary that all blocks are moving or deforming, it is possible to define different groups of blocks each having their own movement. This is in particular useful for multi-body simulations.

To permit CFD simulations on deforming grids it is necessary to re-generate the grid. NSMB includes a remeshing algorithm [1] and recent developments are discussed in more detail in Sect. 5.

3 The B2000++ Solver

B2000++ is a Finite Element Method (FEM) solver which is being developed by SMR Engineering & Development. A wide range of problems in aerospace engineering can be studied, such as global aircraft as well as components or sub-components such as stiffened panels. The element library comprises shell elements, beam elements, point-mass elements, rigid-body elements, as well as 2D and 3D elements. Linear static analysis, linear dynamic analysis, free-vibration analysis and buckling analysis can

be selected, as well as nonlinear static and dynamic analysis. For strength analysis, several failure criteria for isotropic materials and laminated composites are available.

A high computational effectiveness is one of B2000++'s strengths. Symmetric multi-processing (SMP) accelerates the element procedures, taking advantage of today's multi-core CPU's. The open-source matrix solver MUMPS provides distributed parallelism via MPI. Eigen-analysis is carried out with the implicitly restarted Lanczos solver that is implemented in the open-source package ARPACK.

The modular architecture facilitates the implementation of numerical methods. New material and element formulations, essential and natural boundary conditions, and solution methods can be added, requiring no or only a few modifications to the existing code. This flexibility enables the adaptation of B2000++ to specific problems like coupled fully nonlinear FSI.

4 Geometric Multi-region Coupling

To transfer the aerodynamic forces from the CFD wetted surface to the structural FEM model, and to transfer the displacements from the FEM model to the CFD wetted surface, it is necessary to employ a spatial coupling procedure as the CFD and FEM meshes are in general non-matching.

The spatial coupling is implemented within the B2000++ FEM code and is capable of multi-region coupling. As example the F/A-18 wing consists of different control surfaces – inner leading edge flap, outer leading edge flap, trailing edge flap, and aileron – that can move independently. Thus, a multi-region spatial interpolation procedure is utilized where the wing surface and the control surfaces constitute different coupling regions, and C^0 continuity constraints at the coupling region intersections are enforced (Fig. 1).

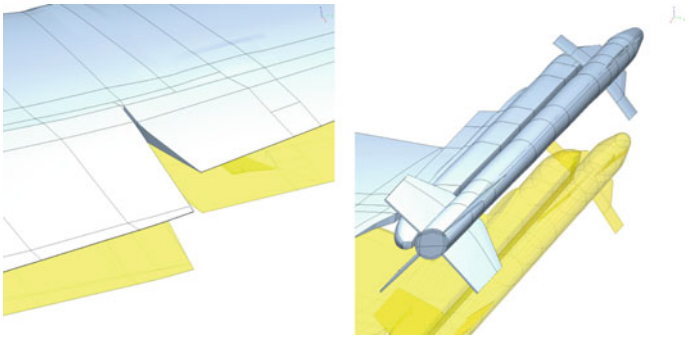

Fig. 1 Undeformed CFD wetted surface (yellow) and deformed CFD surface (silver) at the trailing edge flap and aileron (left) and at the wing tip (right)

4.1 Single-Region Coupling Procedure

The following sets of points are distinguished: The set of structural grid points $\mathscr{S}$, the set of fluid surface points $\mathscr{F}$ where the displacements shall be interpolated, and the set of fluid surface points $\mathscr{P}$ where the displacements are prescribed. $\mathscr{P}$ may be empty. The set of support nodes is $\mathscr{H} = \mathscr{S} \cup \mathscr{P}$, and without loss of generality it is assumed that the coordinates $\mathbf{X}^H$, displacements $\mathbf{u}^H$, and concentrated forces $\mathbf{f}^H$ are arranged as follows:

$$\mathbf{X}^H = \begin{bmatrix} \mathbf{X}^S \\ \mathbf{X}^P \end{bmatrix} \quad ; \quad \mathbf{u}^H = \begin{bmatrix} \mathbf{u}^S \\ \mathbf{u}^P \end{bmatrix} \quad ; \quad \mathbf{f}^H = \begin{bmatrix} \mathbf{f}^S \\ \mathbf{f}^P \end{bmatrix} \tag{1}$$

Let $n = |\mathscr{H}|$ and $m = |\mathscr{F}|$. The volume-spline coupling operator [17] $\mathbf{G}$ is a $m \times n$ matrix

$$\mathbf{G} = \mathbf{AB} \tag{2}$$

where the $m \times (n+1)$ matrix $\mathbf{A}$ is

$$\mathbf{A} = \begin{bmatrix} 1 & ||\mathbf{X}_1^H - \mathbf{X}_1^F|| & ||\mathbf{X}_2^H - \mathbf{X}_1^F|| & \cdots & ||\mathbf{X}_n^H - \mathbf{X}_1^F|| \\ 1 & ||\mathbf{X}_1^H - \mathbf{X}_2^F|| & ||\mathbf{X}_2^H - \mathbf{X}_2^F|| & \cdots & ||\mathbf{X}_n^H - \mathbf{X}_2^F|| \\ 1 & \cdots & \cdots & \cdots & \cdots \\ 1 & ||\mathbf{X}_1^H - \mathbf{X}_m^F|| & ||\mathbf{X}_2^H - \mathbf{X}_m^F|| & \cdots & ||\mathbf{X}_n^H - \mathbf{X}_m^F|| \end{bmatrix} \tag{3}$$

and the $(n+1) \times n$ matrix $\mathbf{B}$

$$\mathbf{B} = (\mathbf{C}^{-1})_{\{\}\{1\}} \tag{4}$$

is a submatrix where the first column is removed from the inverse of the $(n+1) \times (n+1)$ matrix $\mathbf{C}$.

$$\mathbf{C} = \begin{bmatrix} 0 & 1 & 1 & 1 & \cdots & 1 \\ 1 & 0 & ||\mathbf{X}_2^H - \mathbf{X}_1^H|| & ||\mathbf{X}_3^H - \mathbf{X}_1^H|| & \cdots & ||\mathbf{X}_n^H - \mathbf{X}_1^H|| \\ 1 & ||\mathbf{X}_1^H - \mathbf{X}_2^H|| & 0 & ||\mathbf{X}_3^H - \mathbf{X}_2^H|| & \cdots & ||\mathbf{X}_n^H - \mathbf{X}_2^H|| \\ 1 & ||\mathbf{X}_1^H - \mathbf{X}_3^H|| & ||\mathbf{X}_2^H - \mathbf{X}_3^H|| & 0 & \cdots & ||\mathbf{X}_n^H - \mathbf{X}_3^H|| \\ 1 & \cdots & \cdots & \cdots & \cdots & \cdots \\ 1 & ||\mathbf{X}_1^H - \mathbf{X}_n^H|| & ||\mathbf{X}_2^H - \mathbf{X}_n^H|| & ||\mathbf{X}_3^H - \mathbf{X}_n^H|| & \cdots & 0 \end{bmatrix} \tag{5}$$

The displacements $\mathbf{u}^F$ are interpolated as follows:

$$\mathbf{u}^F = \mathbf{G}\mathbf{u}^H \tag{6}$$

The forces acting on the structural grid points and on the constrained fluid surface nodes are obtained by applying the transpose of **G** to the forces on the unconstrained fluid surface mesh nodes:

$$\mathbf{f}^H = \mathbf{G}^T \mathbf{f}^F \tag{7}$$

4.2 Multi-region Coupling Procedure

Two coupling regions A and B are considered where some of the fluid surface mesh nodes belong to both regions (Fig. 2).

To maintain inter-region continuity of the displacements, it is necessary to proceed in three steps. Note that steps 2 and step 3 are interchangeable.

1. $\mathscr{F}$ contains the fluid interface nodes, $\mathscr{S}$ contains the structural nodes of region A and B, and $\mathscr{P} = \emptyset$.
2. $\mathscr{F}$ contains the fluid nodes of region A without the interface nodes, $\mathscr{S}$ contains the structural nodes of region A, and $\mathscr{P}$ contains the fluid interface nodes.
3. $\mathscr{F}$ contains the fluid nodes of region B without the interface nodes, $\mathscr{S}$ contains the structural nodes of region B, and $\mathscr{P}$ contains the fluid interface nodes.

The transfer of the concentrated nodal forces from the fluid wetted surface to the structural grid points is carried out in the opposite order (steps 1 and 2 are interchangeable).

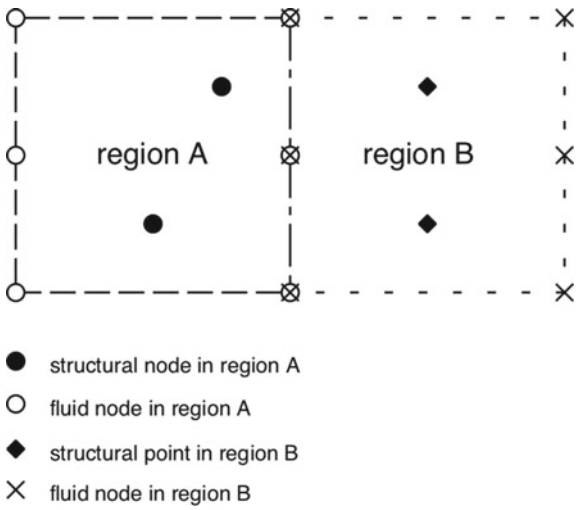

Fig. 2 Two coupling regions with structural points and fluid surface mesh nodes

1. $\mathscr{F}$ contains the fluid nodes of region A without the interface nodes, $\mathscr{S}$ contains the structural nodes of region A. $\mathscr{P}$ contains the fluid interface nodes, for which the calculated forces are added to the fluid forces.
2. $\mathscr{F}$ contains the fluid nodes of region B without the interface nodes, $\mathscr{S}$ contains the structural nodes of region B, and $\mathscr{P}$ contains the fluid interface nodes, for which the calculated forces are added to the fluid forces.
3. $\mathscr{F}$ contains the fluid interface nodes, $\mathscr{S}$ contains the structural nodes of region A and B, and $\mathscr{P} = \emptyset$. The forces that are mapped from $\mathscr{F}$ consist of the fluid forces at these points plus the forces that were mapped in steps 1 and 2 to these points.

Because the operator that maps the forces preserves the sum of forces and is the transpose of the operator that maps the displacements, this spatial coupling procedure is rigid and, therefore, energy-conservative [18], which is important in flutter analysis (in addition, the energy error that is due to the time integration is minimized with the strong coupling approach). The deformed CFD surface is smooth except at the coupling region intersections. It is also possible to enforce zero displacements at coupling region boundaries. For example, the structural FEM model may consist only of a wingbox which is clamped at the root, while the CFD model is a wing-body configuration. In this case, the set $\mathscr{P}$ contains all fluid surface points of the body, and $\mathbf{u}^P = \mathbf{0}$.

4.3 Definition of Coupling Regions

To facilitate the definition of the different coupling regions, the interactive and graphical tool FSCON (Fluid-Structure CONnector) is being used. It allows to select and visualize individual parts of the CFD wetted surface and of the FEM model. For the CFD model, boundary codes are used to select the coupling regions, whereas nodesets, element sets, group codes, etc. are used for the FEM model. Thus, the coupling region definitions are independent of the mesh size and aircraft configuration. Figure 3 shows an example for the Strut Braced Wing configuration. Two different coupling regions are defined, one for the wing and the second one for the strut. To improve the quality of the spatial coupling for the torsional modes, the FEM model is augmented with nodes at the leading and trailing edges that are connected by rigid body elements to the wing box. A subset of the body fluid surface nodes is included in the coupling (colored in orange, the grey part is constrained to zero), since the FEM model is fixed at the symmetry plane and has nonzero displacements at the wing root. In this way possible problems with the re-meshing algorithm are avoided.

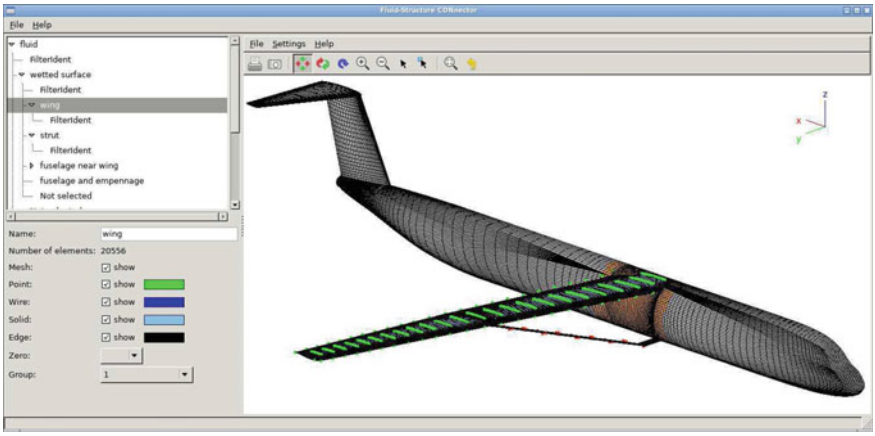

Fig. 3 The FSCON graphical user-interface for the Strut Braced Wing aircraft

5 Remeshing Algorithm

The remeshing algorithm implemented in NSMB is discussed in detail in [2], and is a combination of Volume Spline Interpolation (VSI) [19] and Transfinite Interpolation (TFI). It consists of the following steps:

1. collect information on coordinates and their displacements and create a list of so called prescribed points. These prescribed points are then used to compute the Volume Spline Coefficients by solving a linear matrix systems of equations.
2. compute the displacements of block edges using the VSI method. The advantage of working with the displacements instead of the coordinates is that if the displacement of the edges is close to zero, the displacement in the volume will be close to zero too, and the original coordinates are not changed.
3. use 2D TFI to generate the displacement of the coordinates on the block faces.
4. use 3D TFI to generate the displacement. of the coordinates in the volume.
5. sum the coordinates and displacements to obtain the new mesh.

Several problems were encountered (and solved) for complex grids. For example it might occur that one block edge is shared between 3 blocks or more and not all blocks know about the mesh movement. At the start of a calculation all the information on these shared edges is collected and the displacements between these edges are exchanged during the remeshing process.

The most time consuming part in the process summarized above is the solution of the linear matrix system of equations to compute the Volume Spline Coefficients, and the costs are proportional to $\frac{1}{2}n^2$ with n the number of prescribed points. A large effortwas made to limit the number of prescribed points through a suitable

combination of use of VSI and TFI. Today the remeshing of a F/A-18 third generation mesh having around 50 million points takes less than a minute elapse time on present day HPC clusters.

A recent development in the remeshing procedure concerns the use of the chimera method. The chimera method implemented in NSMB employs blocks inside the structure (that are not computed) to determine intersections between chimera grids. If the structure is moving it means that not only the fluid mesh is moved but one needs also to move the mesh inside the structure. This has been implemented through an exchange of surface displacements between fluid and solid meshes. The second problem concerned the remeshing itself. When moving two aircraft components that have different overlapping grids it might happen that these movements influence each other, leading to negative volumes. The solution to this problem is to perform the remeshing procedure on each chimera grid independent of the other chimera grids.

6 Validation Calculations

6.1 MDO Aircraft

The MDO aircraft is a large transport aircraft with a flexible wing resembling the Airbus 380, and was the result of an EU funded project in the 1990s. The geometry consists of a fuselage and a wing, and the wing has a jig-shape needed for static aero-elastic computations [4]. This case was also used in the EC funded project UNSI (Unsteady Viscous Flow in the Context of Fluid-Structure Interaction) that finished in the year 2000. The results of this project are published in a book [4].

Calculations were made for the so called Case A conditions that are summarized in Table 1. Both the modal approach (considering 10 elastic modes) and the FEM approach using B2000++ were used in the calculations.

The grid employed in the calculations had 123 blocks and about 1.15 million cells, and the surface grid is shown in Fig. 4.

All calculations were made using central space discretization scheme with artificial dissipation, the LU-SGS scheme for the time integration and the $k-\omega$ Menter

Table 1 MDO fuselage-wing Case A conditions

Altitude	37,000	ft
Mach	0.85	
p_∞	21,662.3	Pa
ρ_∞	0.34832	kg/m^3
T_∞	216	K
Re/meter	6.158×10^6	1/m
C_L	0.4581	

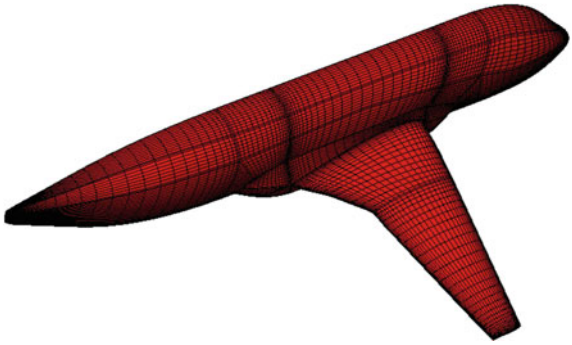

Fig. 4 Grid used for the MDO fuselage-wing calculations

Shear Stress turbulence model [15]. The calculations ran for 7000 steps, and the static wing deformation was executed 5 times, after respectively 4000, 4500, 5000, 5500 and 6000 steps. Figure 5 shows the wing position (including a zoom of the wing tip) at different iterations. The zoom of the wing tip shows clearly the different iteration steps: the first deformation (orange color) shows a large movement upwards followed by a downward movement for the 2nd deformation. The last two deformations (light blue and blue) are close to each other.

Table 2 summarizes the computed angle of attack to reach $C_L = 0.4581$ for this case, and the results are compared with results reported by Saab in [4]. Note that the results obtained by Saab are for the wing only. Figure 6 shows the deformation of the leading and trailing edge of the wing, together with the results obtained by Saab. η

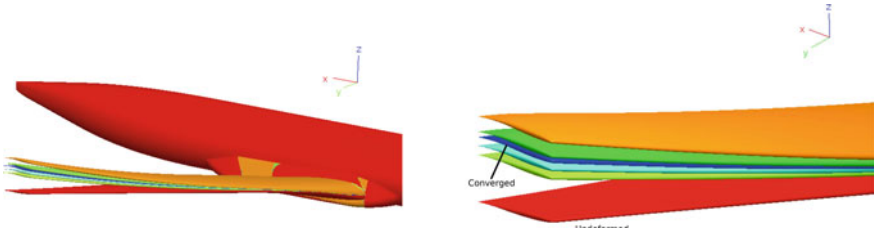

Fig. 5 Static wing deformation of the MDO test case. Colors indicate the iteration (from red (undeformed) via green to blue (last iteration)

Table 2 Computed angle of attack MDO test case A

CFD approach	CSM model	α
Saab Euler	Modal	0.7450
NSMB turbulence	Modal	0.7145
NSMB turbulence	B2000++	0.5330

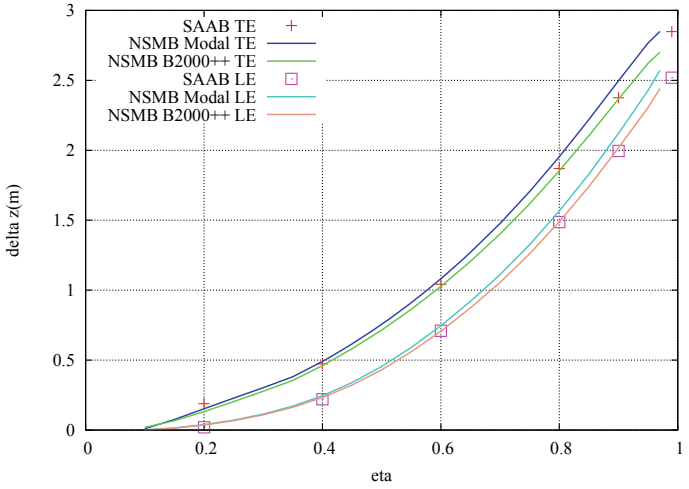

Fig. 6 MDO aircraft test case A: deformation of the leading and trailing edge of the wing

is the normalized y-coordinate (y/y_{max}), with y the coordinate in span direction. As can be seen the NSMB results obtained by using B2000++ are in good agreement with the results by Saab taking into account the different modeling assumptions. One can also observe that the maximum deflection of the leading edge of the wing near the tip is slightly less than 3 m.

Figure 7 shows the computed C_p at 4 stations along the wing, together with the results obtained by Saab. The agreement is good, keeping in mind that the Saab results are obtained for a wing only assuming inviscid flow. Differences between the Saab and NSMB results concern the shock position and the C_p near the trailing edge. Both differences can be explained by the difference in modeling approach.

6.2 AGARD 445.6 Wing

An important problem in the development and validation of dynamic aero-elastic simulation tools is the lack of available experimental data for assessment and validation. Reasons for this are that the experiments by definition are destructive and that they require special models for the correct scaling of the frequencies. One of the most cited experimental test case is the AGARD 445.6 wing [5]. The AGARD445.6 wing, made of mahogany, has a 45° quarter chord sweep, a half span of 2.5 ft, a root chord of 1.833 ft and a constant NACA64A004 symmetric profile. Flutter tests were carried out at the NASA Langley Transonic Dynamics Tunnel, were published in 1963 and re-published in 1987. Various wing models were tested (and broken) in air and Freon-12 for Mach numbers between 0.338 and 1.141.The case most often used

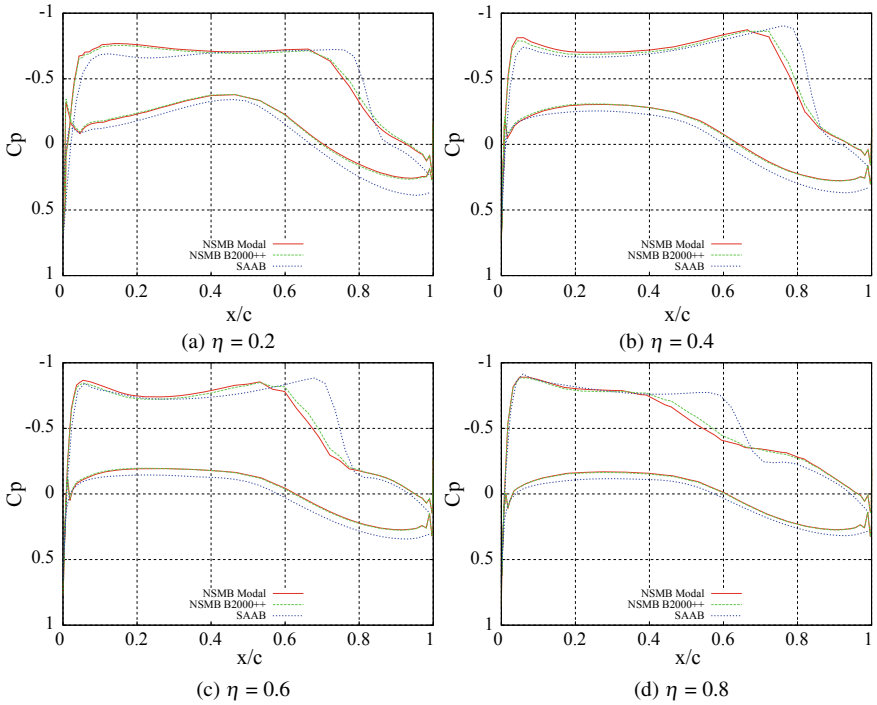

Fig. 7 MDO aircraft test case A: C_p distributions at 4 stations on the wing

Table 3 Material properties AGARD445.6 wing

E_1	3.15106×10^6	Pa
E_2	4.16218×10^8	Pa
G	4.39218×10^8	Pa
ρ	381.98	kg/m^3
ν	0.31	

in the literature is the so called weakened model 3 at zero angle of attack in air. The model was weakened by holes drilled through the surface of the original model to reduce its stiffness.

The linear structural model for the AGARD 445.6 was build by SMR. The material properties for the structural model are summarized in Table 3, and were taken from [20].

In this Table E_1 and E_2 are the moduli of elasticity in the longitudinal and lateral directions, G the shear modulus, ν the Poisson ratio and ρ the wing density. Only the first four mode shapes are considered.

Inviscid calculations were made using a 31 block grid having about 170,000 cells. Grid refinement studies were made indicating that this mesh was sufficient. Table 4

Table 4 AGARD445.6 wing free stream conditions

$Mach$	0.95	
ρ_∞	0.061	kg/m^3
α	0.0	
p_∞	7000, 4600, 3500	Pa
U_∞	381, 309, 269	m/s

lists the free stream values used in the calculations. Three different values of the free stream pressure were used, and due to the change in speed of sounds this results in three different free stream velocities and thus to three different values of the flutter speed index V_f (respectively 0.383, 0.311 and 0.271). The experimental data [5] shows that at $Mach = 0.95$ the flutter boundary is around $V_f = 0.32$, hence the highest pressure condition should yield flutter while for the other 2 conditions no flutter should be found.

All calculations were made using the central scheme with artificial dissipation. The time integration was carried out using dual time stepping [21] employing the 2nd order implicit backward difference scheme. The LU-SGS scheme was used to converge the equations in the inner loop. The unsteady calculations were started from a steady state calculation. A 2% deflection of the first bending moment was given to the structure, and a ramping procedure was used during the first 25 outer time steps to impose this deflection smoothly. Different outer time steps were studied for the case with a free stream pressure of 7000 Pa, indicating that an outer time step of 10^{-3} is a good compromise. Using smaller time steps does not change the results significantly, while the results for larger time steps show differences, in particular in the amplitude of the oscillations.

Figure 8 show the computed C_L as function of time for the different calculations carried out. The left figure shows that flutter is obtained for the highest pressure, as was to be expected. The right figure shows the influence of the CFD-CSM coupling approach for the case with a free stream pressure of 4600 Pa. The weak coupling approach (couple the fluid and structure only each outer time step) leads to undamped oscillations while with the strong coupling approach (couple the fluid and structure each step in the inner time stepping loop) the oscillations are not amplified. With the strong coupling approach it is possible to switch off the CFD-CSM coupling after a certain number of inner loop steps. Performing the coupling only the first 25 steps of the inner time stepping loops yields results close to the results obtained by making the coupling each step.

7 Strut Braced Wing Aircraft

In the frame of the European Funded H2020 project AGILE (Aircraft 3rd Generation MDO for Innovative Collaboration of Heterogeneous Teams of Experts) [6] aero-

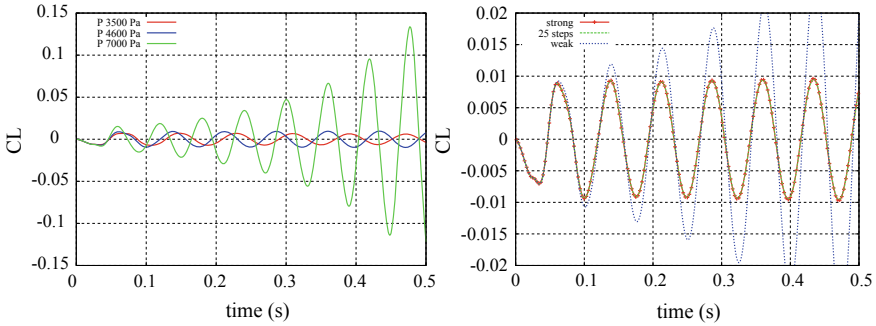

Fig. 8 Results AGARD445.6 case, left lift coefficient as function of time for different free stream pressures, right influence of coupling approach on the lift coefficient for a free stream pressure of 4600 Pa

elastic simulations were made for a Strut Braced Wing aircraft. The Strut Braced Wing (SBW) aircraft has received much attention over the last 10 years due to its potential to reduce emissions. However the SBW aircraft also poses several challenges, in particular the strong coupling between aerodynamics and structures [22]. The SBW aircraft designed in the AGILE project concerns a 90-seat passenger aircraft. The design choice's and the top level aircraft requirements are discussed in the paper by Torrigiani [22]. Navier Stokes simulations were carried out for different wing configurations, showing that a wing with a super-critical airfoil and having a 16° sweep angle is the most efficient (compared to the initial configuration having a 0° sweep angle and a NACA009 airfoil). However these high-fidelity simulations did not take into account the deformation of the strut and the wing due to the aerodynamic loads.

An aero-elastic tool chain has been set-up composed of the PROTEUS tool developed at the Delft University of Technology, the AMLoad tool developed by the Netherlands Aerospace Centre (NLR), the FSCON tool discussed in this paper and the NSMB CFD solver.

7.1 PROTEUS

PROTEUS is an aeroelastic tool, developed at the Delft University of Technology. Figure 9 depicts the schematic representation of the framework of PROTEUS. To start with, the wing is discretized into multiple sections in the spanwise direction. For each spanwise section, one or more laminates can be defined in the chord wise direction. Using the laminate properties and the cross sectional geometry, a cross sectional modeler especially developed to deal with anisotropic shell cross-sections, converts the three-dimensional wing into a Timoshenko beam element. A geometrically nonlinear aeroelastic simulation is performed by coupling the nonlinear beam model to a vortex lattice aerodynamic model. A linearized dynamic aeroelastic anal-

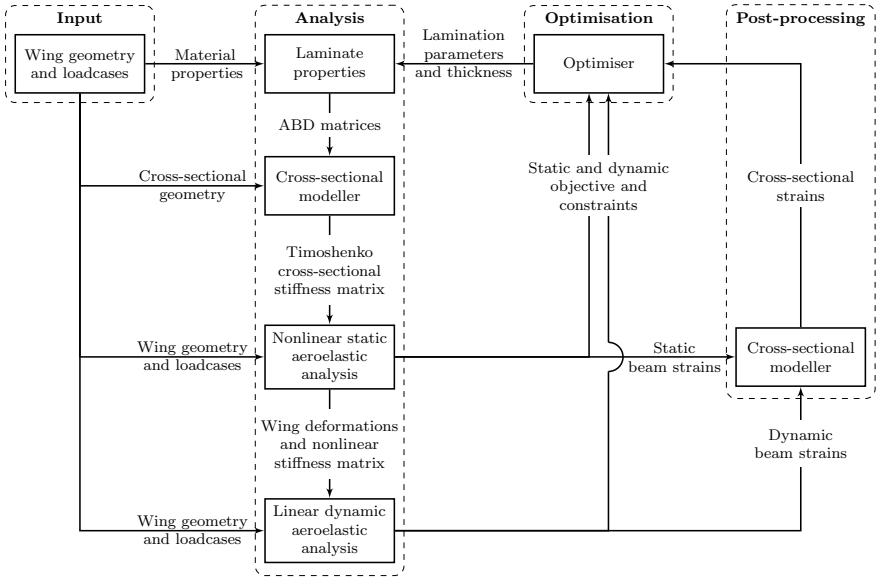

Fig. 9 Framework of PROTEUS [23]

ysis is carried out around the nonlinear static equilibrium solution. The strains in the three-dimensional wing structure are obtained through the cross sectional modeler. Based on the applied strains, strength, buckling and the fatigue properties of the wing are calculated and fed to the optimizer as constraints. Since analytical derivatives of the objective and constraints with respect to the design variable are calculated with PROTEUS, an efficient gradient based optimizer can be used for optimization. A detailed description of PROTEUS is given the papers by Werter and De Breuker [23, 24].

7.2 Aero-elastic Coupling

The aeroelastic chain used for the Strut Braced Wing aircraft in the AGILE project starts with PROTEUS, in which the aeroelastic stiffness and thickness optimization of the wing structure is carried out. The material properties used for optimization are given in Table 5. The optimization problem is shown in Table 6. The objective of the study is to minimize the structural weight of the wing. The wing is divided into 8 sections; 7 sections along the spanwise direction of the main wing and 1 section representing the strut. The sections each have 4 laminates: one laminate each for top and bottom skin, and for front and rear spar. This results in 32 unique laminates. Laminates can be unsymmetric and balanced but are chosen to be symmetric and

Table 5 Material properties of AS4/3506 carbon/epoxy

Property	Value (GPa)
E_{11}	147
E_{22}	10.3
G_{12}	7
ν_{12}	0.27
X_t	2.28
X_c	1.72
Y_t	0.057
Y_c	0.23
S	0.076

Table 6 Optimization setup

Type	Parameter	# responses
Objective	Minimize wing mass	1
Design variables	Lamination parameter Laminate thickness	279
Constraints	Laminate feasibility	140
	Static strength	384/loadcase
	Buckling	1792/loadcase
	Aeroelastic stability	10/loadcase
	Local angle of attack	22/loadcase

unbalanced in this study. Every laminate is described by eight lamination parameters and one thickness variable, resulting in a total of 288 design variables.

To ensure that lamination parameters represent a realistic ply distribution, feasibility equations formulated by Hammer et al. [25], Raju et al. [26] and Wu et al. [27] are applied. The modified Tsai Wu failure envelope [28] suitable for lamination parameter domain is used to assess the static strength of the laminate. The stability of the panel in buckling is based on idealized buckling model formulated by Dillinger et al. [29]. To guarantee the static and dynamic aeroelastic stability of the wing, the real part of the eigenvalues of the state matrix should be less than zero. The local angle of attack is constrained to a maximum of 12° and a minimum of −12°.

Table 7 gives the information on the loadcases which are used for the current study. These loadcases, represent the flutter boundary, 2.5 g symmetric pull up maneuver and −1 g symmetric push down maneuver.

The optimized stiffness and mass matrices are then fed to AMLoad in which a full aircraft MSC Nastran structural model is made in which the wing and strut are represented by matrices.

Table 7 List of loadcases

Loadcase ID	V (m/s)	Altitude (m)	Load factor
1	264	11,000	1
2	230	11,000	2.5
3	230	11,000	−1

7.3 AMLoad

Within the framework of the strut-braced wing, AMLoad, in-house developed by the Netherlands Aerospace Centre (NLR), was used both to convert stiffness and mass matrices obtained by PROTEUS to the B2000++ solver and to provide low/mid-fidelity static aeroelastic solutions. AMLoad is based on the vortex lattice panel aerodynamics, and includes correction factors for airfoil camber and for additional skin-friction drag components. As well known, panel aerodynamics do not take into account viscous effects meaning it cannot predict flow separation due to shocks at higher Mach numbers or high incidence angles. In order to increase the accuracy of the design by including viscous effects, high fidelity FSI simulations have been made using the NSMB CFD solver. To establish the connection within the framework, the output from the modal analysis using AMLoad's structural model is used including the optimized stiffness and mass matrices from PROTEUS.

Using the matrices inherently means that the detailed finite element properties are non-existing anymore. However, in order to perform high fidelity aeroelastic simulations, a 3D structural model is required in order to spline the model to the CFD mesh. Since it is not possible and common to reverse engineer the full detailed finite element model based on only the matrices another solution is proposed. In this solution, the simplified structural MSC Nastran model (existing of nodes in combination with the Direct Matrix Input (DMIG) cards) is extended using Rigid Body Elements (RBE's). The RBE2 element is a rigid body connected to an arbitrary number of grid points. In this case, the structural nodes which include the structural dynamic matrices are connected to surrounding grid points representing the box structure of the wing (see Fig. 10). The independent degrees of freedom of the surrounding nodes are the six components of motion at a single grid point.

Fig. 10 Modeshapes of the 3D structural dynamic MSC Nastran model including RBE2 elements for splining, (left). First wing bending mode (clamped BC) and (right) first strut bending (clamped BC)

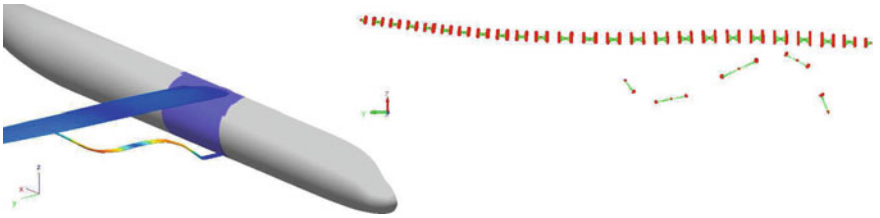

Fig. 11 Structural bending mode splined to CFD model (left) and structural model (right)

Fig. 12 Static aeroelastic solution under conditions; M = 0.78, angle of attack = 10°, altitude 11,000 m

These methods are applied for the full wing and strut with an increasing density of structural nodes along the span. This density increase along the span increases the accuracy of the mode shapes used in the high fidelity aeroelastic simulations, see Fig. 11.

A restriction of using the rigid elements is the fact that local modes, e.g. local buckling modes or wing torsion at a specified spanwise location, cannot be captured accurately. However, these kind of local modes are not of significant influence for the aeroelastic simulation and therefore do not compromise the results. In addition to the conversion of the structural model, static Aeroelastic solutions have been computed by AMLoad as input to a mission simulation tool (the so called flexible polar). Figure 12 shows the static aeroelastic deformation obtained using the optimized structural model from Proteus. The deformation at the tip is about 95 cm using vortex lattice panel methods.

7.4 Results

The geometric coupling tool described in 4 was used to couple the CFD to the FEM model, and the result is shown in Fig. 3. CFD simulations using NSMB were then made for different Mach numbers and different angles of attack. The freestream conditions are summarized in Table 8 and angles of attack considered were $-5°$, $-2.5°$, $0°$, $2.5°$, $5°$ and $10°$. All NSMB calculations used the same set-up: the 2nd order Roe scheme for the space discretization, the LU-SGS semi-implicit scheme for the time integration, and the $k - \omega$ Menter Shear Stress model to model

Table 8 Strut Braced Wing calculation conditions

Altitude	11,000	m
Mach	0.70, 0.78, 0.88	
α	−5.0, −2.5, 0.0, 2.5, 5.0, 10.0	°
p_∞	22,700	Pa
T_∞	217	K

the turbulence. All calculations were made on a grid having 327 blocks and about 4.9 million grid cells. The calculations without fluid structure interaction were run for 8000 steps. The aero-elastic calculations were first run for 3000 steps, and then the aero-elastic coupling was taken into account 10 times every 500 steps. Since the first deformations are in general overestimated under-relaxation was used in the first three coupling steps (the computed displacements were multiplied with factors of 0.5, 0.75 and 0.90 respectively).

Figure 13 shows for the Mach = 0.78, $\alpha = 10°$ calculation the wing and strut positions at the start, after 5 deformations and at the end of the simulation (10 deformations). One can observe that the difference in wing and strut positions after 5 and 10 deformations is small. Table 9 shows that the wing tip deformation after 10 deformations was 0.578 m, after 5 deformations this was equal to 0.571 m.

Figure 14 shows a front view of same case, with the undeformed wing on the left and the deformed wing on the right. One can clearly observe the upward movement of the wing tip for the deformed configuration.

Figure 15 shows the wing tip profile, whereby the deformed profile has been translated 0.59 m in z-direction to match the undeformed wing. One can observe a small wing twist and a slightly forward movement of the wing.

For several Mach numbers the same calculations were also made using AMLoad to allow a comparison of Low Fidelity (LowFi) and High Fidelity (HighFi) methods. Table 9 summarizes the computed vertical displacement as function of the Mach

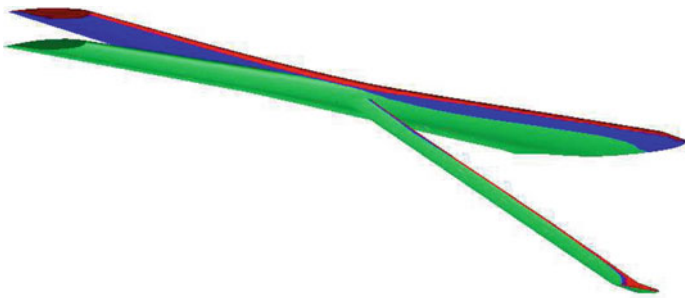

Fig. 13 Wing and Strut position, case Mach = 0.78, $\alpha = 10°$: green: undeformed position, blue: after 5 deformations, red: final position

Table 9 Wing tip maximum vertical displacement in meters, Strut Braced Wing configuration

α	LowFi	HighFi	LowFi	HighFi	LowFi	HighFi	HighFi
	$M = 0.20$	$M = 0.20$	$M = 0.60$	$M = 0.60$	$M = 0.78$	$M = 0.78$	$M = 0.88$
−5.0	−0.036	−0.026	−0.259	−0.160	−0.189	−0.153	
−2.5	0.019	0.026	−0.019	0.050	0.026	0.048	0.042
0.0	0.073	0.079	0.228	0.267	0.241	0.253	0.069
2.5	0.128	0.133	0.472	0.490	0.457	0.457	0.166
5.0	0.182	0.186	0.715	0.715	0.672	0.602	0.346
10.0	0.291	0.291	1.203	1.038	1.103	0.578	

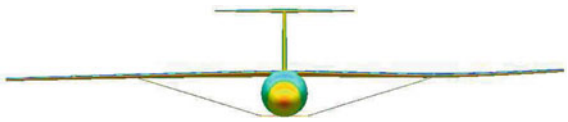

Fig. 14 Front view of the Strut Braced Wing aircraft, right: undeformed configuration, left: deformed configuration, case Mach = 0.78, $\alpha = 10°$

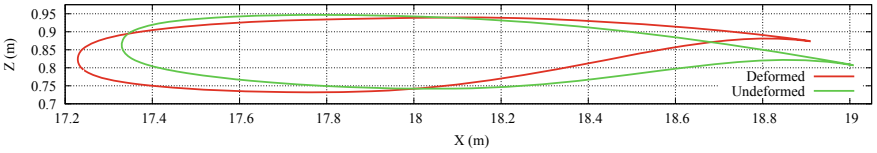

Fig. 15 Wing tip profile of the undeformed and deformed configuration, case Mach = 0.78, $\alpha = 10°$

number and angle of attack. One can observe that at $Mach = 0.20$ the computed displacements using the low and high fidelity methods are very close, except at $\alpha = -5°$. At $Mach = 0.60$ and in particular at $Mach = 0.78$ the displacements predicted using the high fidelity method at an angle of attack of 10° are lower than the low fidelity results. It was observed that at this angle of attack the flow on the wing is largely separated, see Fig. 16, and this is not taken into account in the AMLoad simulations.

For the $Mach = 0.88$ case there are shock waves on the wing, followed by a shock induced separation even at low angles of attack and for this reason displacements are smaller than the computed displacements at $Mach = 0.78$.

Figure 17 shows the computed aerodynamic coefficients for the different Mach numbers, using both AMLoad and NSMB with and without aero-elastic deformation of the wing and strut. Accounting for wing deformation reduces slightly the lift coefficient but also leads to an important reduction in the drag coefficient. As a result the aerodynamic efficiency is slightly higher, in particular for the higher incidence angles.

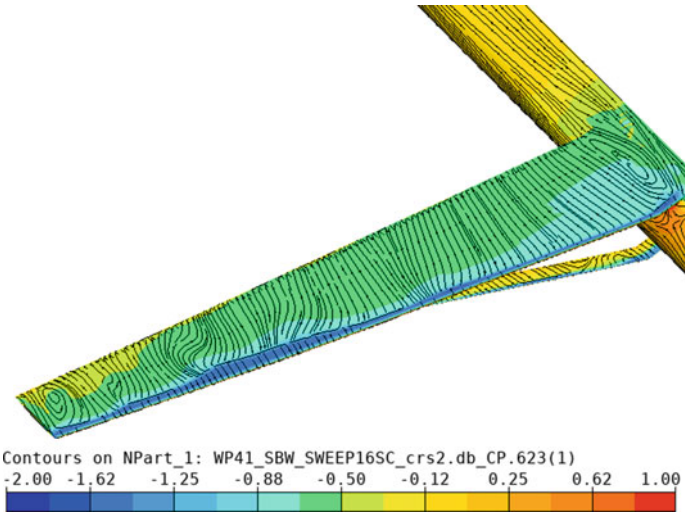

Fig. 16 C_p and skin friction lines, case Mach = 0.78, $\alpha = 10°$

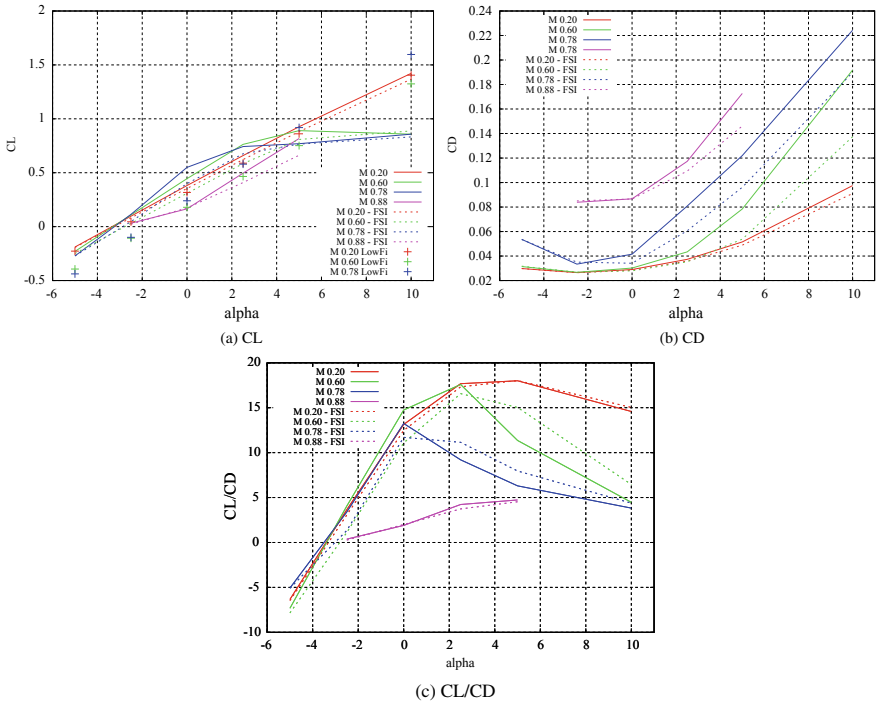

(a) CL (b) CD

(c) CL/CD

Fig. 17 Computed aerodynamic coefficients with and without wing deformation

When looking to the drag coefficient of the strut it can be observed that it is comparable to the drag coefficient without deformation at angles of attack below 0°, but it is 5–10% lower at higher angles of attack.

8 Conclusions

Developments made to the NSMB CFD solver to improve the aero-elastic simulation capability were presented. NSMB was successfully coupled to the B2000++ open-source Finite Element Analysis Environment. A discussion on the geometrical coupling tool to transfer the aerodynamic loads from the CFD mesh to the structure FEM model, and to transfer the displacements from the FEM model back to the CFD grid was presented.

The aero-elastic simulation environment was used to simulate the MDO aircraft and the AGARD445.6 wing test cases, and results are in good agreement with results found in literature.

Finally the aero-elastic simulation environment was used to compute a Strut Braced Wing configuration. For this case the structural model was build using the PROTEUS software developed at the Delft University of Technology. This structural model was then translated into a Nastran model using the AMLoad software developed at the Netherlands Aerospace Centre NLR. The geometrical coupling tool discussed in this paper was then used to couple the FEM and CFD model. Calculations were made for various Mach numbers. Accounting for aero-elasticity reduced the lift and drag coefficient, but led to an increase in aerodynamic efficiency for higher Mach numbers. It was also observed that taking into account aero-elasticity led to a reduction of the drag of the strut. Comparing low and high fidelity simulation methods shows that low fidelity methods predict C_L values close to the high fidelity methods for low Mach numbers; however large differences appear when shock wave and flow separations occur, in particular at high Mach numbers and high incidence angles.

Acknowledgements The research on the Strut Braced Wing configuration presented in this paper has been performed in the framework of the AGILE project (Aircraft 3rd Generation MDO for Innovative Collaboration of Heterogeneous Teams of Experts) and has received funding from the European Union Horizon 2020 Programme under grant agreement no. 636202. The Swiss participation in the AGILE project was supported by the Swiss State Secretariat for Education, Research and Innovation (SERI) under contract number 15.0162. The authors are grateful to the partners of the AGILE consortium for their contribution and feedback.

References

1. Guillaume M., Gehri A., Stephani P., Vos J., & Manadanis G. (2010). *Fluid structure interaction simulation on the F/A-18 vertical tail*. AIAA-2010-4613, Chicago.
2. Guillaume, M., Gehri, A., Stephani, P., Vos, J., & Mandanis, G. (2011). F/A-18 vertical buffeting calculations using unsteady fluid structure interaction. *The Aeronautical Journal*, *115*(1166), 285–294.
3. http://www.smr.ch/products/b2000/.
4. Haase, W., Selmin, V. and Winzell, B. (2003). *Progress in computational fluid-structure interaction*. Notes on Numerical Fluid Mechanics and Multidisciplinary Design, vol. 81. Springer.
5. Yates, E. C., Jr. (1987). *AGARD Standard aero-elastic configurations for dynamic response. I: Wing 445.6*. AGARD R-765, 1988. Also published as NASA TM-100492.
6. Ciampa, P. D., & Nagel, B. (2018). AGILE the next generation of collaborative MDO: Achievements and open challenges. *AIAA paper*, *2018–3249*.
7. de C. Henshaw, M. J., Badcock, K. J., Vio, G. A., Allen C. B, Chamberlain, J., Kaynes, I., et al. (2007). Non-linear aeroelastic prediction for aircraft applications. *Progress in Aerospace Sciences, 43*.
8. Afonso, F., Vale, J., Oliveira, E., Lau, F., & Suleman, A. (2017). A review on non-linear aeroelasticity of high aspect-ratio wings. *Progress in Aerospace Sciences*, *89*, 40–57.
9. Mian, H. H., Wang, G., & Ye, Z.-Y. (2014). Numerical investigation of structural geometric nonlinearity effect in high-aspect-ratio wing using CFD/CSD coupling approach. *Journal Fluids Structures*, *49*, 186–201.
10. Vos, J. B., Rizzi, A. W., Corjon, A., Chaput, E., & Soinne, E. (1998). Recent advances in aerodynamics inside the NSMB (Navier-Stokes Multiblock) consortium. *AIAA paper*, *98–0225*.
11. Vos, J. B., Sanchi, S., & Gehri, A. (2013). Drag prediction workshop 4 results using different grids including near-field/far-field drag analysis. *Journal of Aircraft*, *50*(5), 1616–1627.
12. Vos, J. B., Bourgoing, A., Soler, J., & Rey, B. (2015). Earth re-entry capsule CFD simulations taking into account surface roughness and mass injection at the wall. *International Journal of Aerodynamics*, *5*(1), 1–33.
13. Hoarau, Y., Pena, D., Vos, J. B., Charbonnier, D., Gehri, A., Braza, M., et al. (2016). Recent developments of the Navier Stokes Multi Block (NSMB) CFD solver. *AIAA Paper*, *2016–2056*.
14. Spalart, P. R., & Allmaras, S. R. (1992). A one-equation turbulence model for aerodynamic flows. *AIAA Paper*, *92–0439*.
15. Menter, F. R. (1993). Zonal two equation $k-\omega$ turbulence models for aerodynamic flows. *AIAA paper*, *93–2906*.
16. Langtry, R., & Menter, F. (2009). Correlation-based transition modeling for unstructured parallized computational fluid dynamic codes. *AIAA Journal*, *47*, 2894–2907.
17. Hounjet, M. H. L., & Meijer, J. J. (1995). *Evaluation of elastomechanical and aerodynamic data transfer methods for non-planar configurations in computational aeroelastic analysis* (pp. 18–19). TP 95690U, National Aerospace Laboratory NLR, Amsterdam, The Netherlands.
18. Beckert, A. (1997). Ein Beitrag zur Strömungs-Struktur-Kopplung für die Berechnung des aeroelastischen Gleichgewichtszustandes, Forschungsbericht-Deutsches Zentrum für Luft und Raumfahrt.
19. Spekreijse, S. P., Prananta, B. B., & Kok, J. C. (2002). *A simple , robust and fast algorithm to compute deformations of multi-block structured grids*. NLR-TP-2002-105.
20. Goura, G. S. L. (2001). *Time marching analysis of flutter using computational fluid dynamics*. Ph.D. thesis, University of Glasgow.
21. Jameson, A. (1991, June). Time dependent calculations using multigrid, with applications to unsteady flows past airfoils and wings. *AIAA Paper*, *91–1596*.
22. Torrigiani, F., Bussemaker, J., Ciampa, P. D., Fiorite, M., Tomasella, F., Aigner, B., et al. (2018). *Design of the Strut Braced Wing Aircraft in the AGILE collaborative MDO framework*. ICAS.
23. Werter, N. P. M., & De Breuker, R. (2016). A novel dynamic aeroelastic framework for aeroelastic tailoring and structural optimisation. *Composite Structures*, *158*, 369–386.

24. Werter, N. P. M., & De Breuker, R. (2017). Continuous-time state-space unsteady aerodynamic modeling for efficient loads analysis. *AIAA Journal*, *56*(3), 905–916.
25. Hammer, V. B., Bendsøe, M. P., & Pedersen, P. (1997). Parametrization in laminate design for optimal compliance. *International Journal of Solids and Structures*, *34*(4), 415–434.
26. Gangadharan, R., Wu, Z., & Weaver, P. (2014). On further developments of feasible region of lamination parameters for symmetric composite laminates. In *55th AIAA/ASMe/ASCE/AHS/SC structures, structural dynamics, and materials conference*.
27. Wu, Z., Gangadharan, R., & Weaver, P. (2015). Framework for the buckling optimization of variable-angle tow composite plates. *AIAA Journal*, *53*(12), 3788–3804.
28. Khani, A., IJsselmuiden, S. T., Abdalla, M. M., & Gürdal, Z. (2011). Design of variable stiffness panels for maximum strength using lamination parameters. *Composites Part B: Engineering*, *42*(3), 546–552.
29. Dillinger, J. K. S., Klimmek, T., Abdalla, M. M., & Gürdal, Z. (2013). Stiffness optimization of composite wings with aeroelastic constraints. *Journal of Aircraft*, *50*(4), 1159–1168.